Electronic Supplementary Information

Experimental section

Materials: Lanthanum acetate hydrate ($C_6H_9O_6La{\cdot}xH_2O$), sodium fluoride (NaF), sodium citrate dehydrate ($C_6H_5Na_3O_7{\cdot}2H_2O$), Lithium perchlorate ($LiClO_4$), nitroferricyanide (III) dihydrate ($Na_2Fe(CN)_5NO{\cdot}2H_2O$), sodium sulfate ($Na_2SO_4$), and Nafion (5wt%) sodium were purchased from Aladdin Ltd. in Shanghai. Para-(dimethylamino) benzaldehyde ($C_9H_{11}NO$), sodium salicylate ($C_7H_5O_3Na$), hydrazine hydrate ($N_2H_4{\cdot}H_2O$), sodium hypochlorite (NaClO), sodium hydroxide (NaOH), hydrochloric acid (HCl), ethanol (CH_3CH_2OH), and carbon paper (CP; TGP-H-060) were bought from Beijing Chemical Corporation. The ultrapure water was purified through a Millipore system used throughout all experiments.

Sample preparation: Briefly, $C_6H_9O_6La{\cdot}xH_2O$ (2 mmol) dissolved in 10 mL water and added 20 mL aqueous solution containing 2 mmol of $C_6H_5Na_3O_7{\cdot}2H_2O$. The solution was stirred vigorously for 30 min and 30 mL of NaF (25 mmol) solution was introduced into the above solution. Then the mixture was sealed in a 100 mL Teflon-lined autoclave and maintained at 180 ^oC for 24 h. After the autoclave cooled down at room temperature naturally, the resulting product was collected by centrifugation, and washed with water and ethanol for several times, followed by drying at 80 ^oC for 12 h under vacuum conditions. The La_2O_3 was prepared by the above method without addition of NaF, then annealed at 700 ^oC for 4 h.

Characterizations: XRD data were obtained from a LabX XRD-6100 X-ray diffractometer with Cu Kα radiation (40 kV, 30 mA) of wavelength 0.154 nm (SHIMADZU, Japan). SEM images were collected on a field-emission scanning electron microscopy (HITACHI SU8100, Tokyo, Japan). TEM images were collected on a transmission electron microscopy (HITACHI H-8100, Tokyo, Japan). AFM images were acquired on a Bruker MultiMode-8 atomic force microscopy (Bruker, USA). Raman spectra were obtained by a Renishaw InVia confocal Raman microprobe under 532 nm laser excitation. XPS measurements were performed on an ESCALABMK II X-ray photoelectron spectrometer using Mg as the exciting source. The absorbance data of spectrophotometer were collected on a SHIMADZU UV-2700 ultraviolet-visible (UV-Vis) spectrophotometer. The ion chromatography data were collected on Thermofisher ICS 5000 plus using the dual temperature heater, injection valve, conductivity detector, AERS 500 Anions suppressor. A gas chromatograph (SHIMADZU, GC-2014C) equipped with MolSieve 5A column and Ar carrier gas was used for H_2 quantifications. ^1H NMR experiments were carried out at 303 K for 5% w/v sample solution in DMSO-d6. The spectral windows were set to 12.5 kHz (25 ppm), a total of 16 scans were recorded, a π/2 pulse length of 11.6 μs and 64 K data points with 3 s recycle delay for each sample. Topspin

software version is 3.5 pl6. All ^{1}H chemical shifts are referenced to the resonances of DSS standard (δ = 0.00).

Electrocatalytic N_2 reduction measurements: The N_2 reduction experiments were carried out in a two-compartment cell under ambient condition, which was separated by Nafion 117 membrane. The membrane was treated in H_2O_2 (5%) aqueous solution at 80 °C for 1 h and dipped in 0.1 M H_2SO_4 at 80 °C for another 1 h. And finally, the membrane was treated in ultrapure water at 80 °C for 6 h. The electrochemical measurements were conducted on a CHI660E electrochemical analyzer (CH Instruments, China). A three-electrode system was used to test the electrocatalytic performance in 0.5 M $LiClO_4$ (30 mL) at controllable applied potentials using LaF_3 deposited on CP (LaF_3/CP; LaF_3 loading: 0.1 mg cm^{-2}; CP area: 1 x 1 cm^2) as the working electrode, Ag/AgCl (filled with saturated KCl solution) as the reference electrode, and graphite rod as the counter electrode. All potentials were reported on a RHE scale. For comparison, La_2O_3/CP was also prepared using the same catalyst loading. The potentials reported in this work were converted to RHE scale via calibration with the following equation: E (vs RHE) =E (vs Ag/AgCl) + 0.197 + 0.059 × pH. For N_2 reduction experiments, the electrolyte solution (0.5 M $LiClO_4$) was bubbled with N_2 for 30 min before the measurement.

Determination of NH_3: Concentration of produced NH_3 was determined by spectrophotometry measurement with indophenol indicator.[1] In detail, 4 mL of post-tested solution was got from the electrochemical reaction vessel. Then 50 μL of NaClO (4.5%) and NaOH (0.75 M), 500 μL of $C_7H_5O_3Na$ (0.4 M) and NaOH (0.32 M) and 50 μL of 1 wt% $Na_2Fe(CN)_5NO{\cdot}2H_2O$ were added into the above solution. Absorbance measurements were performed after 1 h in dark. The concentration-absorbance curve was calibrated using the standard NH_4Cl solution with NH_3 concentrations of 0.0, 0.15, 0.20, 0.30, 0.50, and 0.60 μg mL^{-1} in 0.5 M $LiClO_4$. Typically, 500 μg mL^{-1} NH_3 solution was prepared (0.786 g NH_4Cl dissolved in 0.5 M $LiClO_4$) and diluted to 5 μg mL^{-1}. Then, 0.0, 0.3, 0.4, 0.6, 1.0, and 1.2 mL NH_3 solution with concentration of 5 μg mL^{-1} were poured into 10 mL test tubes and separately diluted to 10 mL with 0.5 M $LiClO_4$. Identical experiments were conducted using Na_2SO_4 electrolyte and concentration-absorbance curve was calibrated using the standard NH_4Cl solution with NH_3 concentrations of 0.0, 0.05, 0.10, 0.15, 0.20, and 0.30 μg mL^{-1} in 0.1 M Na_2SO_4. The fitting curves show good linear relation of absorbance value with NH_3 concentration by three times independent calibrations.

Determination of N_2H_4: The N_2H_4 presented in the electrolyte was estimated by the method of Watt and Chrisp[2]. A mixed solution of $C_9H_{11}NO$ (5.99 g), HCl (concentrated, 30 mL) and

ethanol (300 mL) was used as a color reagent. Typically, 5 mL electrolyte was removed from the cathodic chamber, after that, added into 5 mL above prepared color reagent and stirring 20 min at room temperature. The absorbance of the resulting solution was measured at 455 nm. The concentration absorbance curves were calibrated using standard N_2H_4 solution with a series of concentrations. The fitting curve shows good linear relation of the absorbance with N_2H_4 concentration ($y = 0.748\ x + 0.033$, $R^2 = 0.999$).

Determination of FE and NH_3 yield: The FE for N_2 reduction was defined as the amount of electric charge used for synthesizing NH_3 divided the total charge passed through the electrodes during the electrolysis. The total amount of NH_3 produced was measured using colorimetric methods. Assuming three electrons were needed to produce one NH_3 molecule, the FE could be calculated as follows:

$$FE\ (NH_3) = 3 \times F \times [NH_3] \times V / (17 \times Q) \times 100\%$$

The rate of NH_3 formation was calculated using the following equation:

$$NH_3\ \text{yield} = [NH_3] \times V / (m_{cat.} \times t)$$

The amount of NH_3 was calculated as follows:

$$m_{NH3} = [NH_3] \times V$$

Where F is the Faraday constant, $[NH_3]$ is the measured NH_3 concentration, V is the volume of the electrolyte in the cathodic chamber, Q is the total quantity of applied electricity, t is the reduction time, and $m_{cat.}$ is the loaded mass of catalyst on carbon paper.

The FE of H_2 was calculated as below:

$$FE\ (H_2) = 2 \times F\ V_{H2} \times G \times p_0 / (R \times T \times Q) \times 100\%$$

Where V_{H2} is the volume concentration of H_2 in the exhaust gas from the electrochemical cell (GC data), G is the gas flow rate (mL min^{-1}), Q is the total quantity of applied electricity, $p_0 = 1.01 \times 10^5$ Pa, T = 298.15 K, and R = 8.314 J mol^{-1} K^{-1}.

Calculation details: First-principles calculations based DFT were performed with the generalized gradient approximation (GGA)[3] in the form of the Perdew, Burke, and Ernzerhof (PBE)[4] exchange-correlation functional, as implemented in the Dmol[3] package.[3,5] A six atom layers (111), (300), (1-10), (100), (001), and (110) surfaces of LaF_3 were modelled with 20 Å vacuum space to avoid the interaction form nearby layers. Layers 1 to 2 are surface layers, layers 3 to 5 are central layers. Structural relaxation was performed until the convergence criteria for energy were set to be 10^{-5} eV, and 0.004 Ha $Å^{-1}$ was adopted for the total energy calculations. The N_2 dissociation minimum energy path (MEP) was obtained by LST/QST

tools in DMol^3 code.[6] The Brillouin zone integration was performed with 3 × 3 × 2 Γ-centred Monkhorst-Pack k-point meshes in geometry optimization. We examined a series of facets of LaF_3, including (300), (111), (1-10), (100), (001), and (110).

Frequencies of each complex were calculated after geometry optimization, and the free energy was obtained as follows:

$$\triangle G = \triangle E + \triangle ZPE - T\triangle S + \triangle G_u + \triangle G_{pH}$$

where $\triangle E$, $\triangle ZPE$ and $\triangle S$ are the difference in DFT-calculated total energy change, zero-point energy and the change in entropy between the products and reactants, respectively. T is the temperature (298.15 K). $\triangle G_U = -neU$, where n is the number of transferred charge, and U is the electrode potential with respect to the normal hydrogen electrode. $\triangle G_{pH}$ is the correction H^+ free energy by the concentration, which can be calculated through $\triangle G_{pH} = 0.059 \times pH$ (the value of pH is assumed to be zero in this work). The N_2 adsorption energy is defined as:

$$E_{ads} = E_{N2/substrate} - E_{substrate} - E_{N2}$$

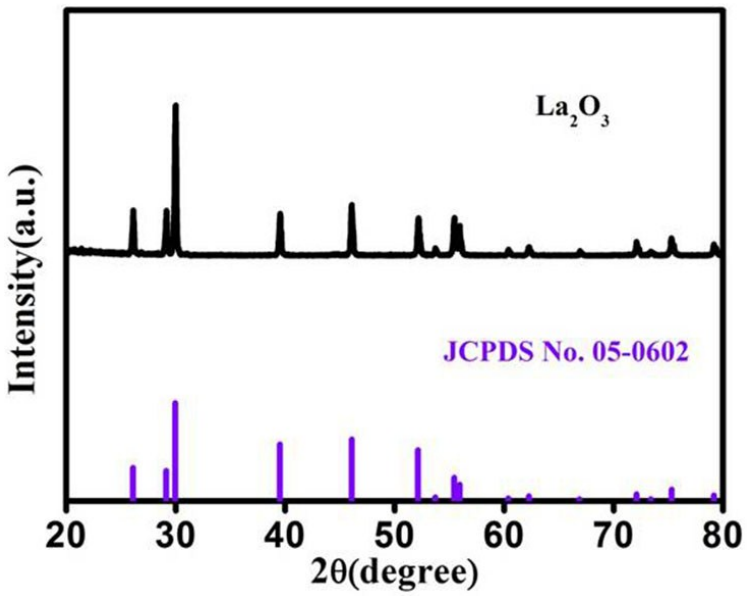

Fig. S1. XRD patterns of La_2O_3.

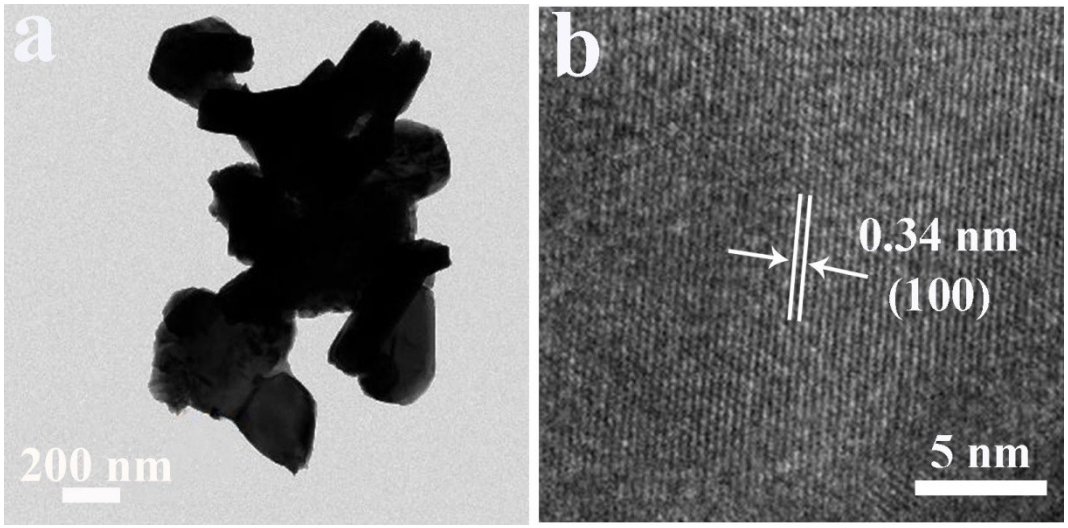

Fig. S2. (a) TEM and (b) HRTEM images of La_2O_3.

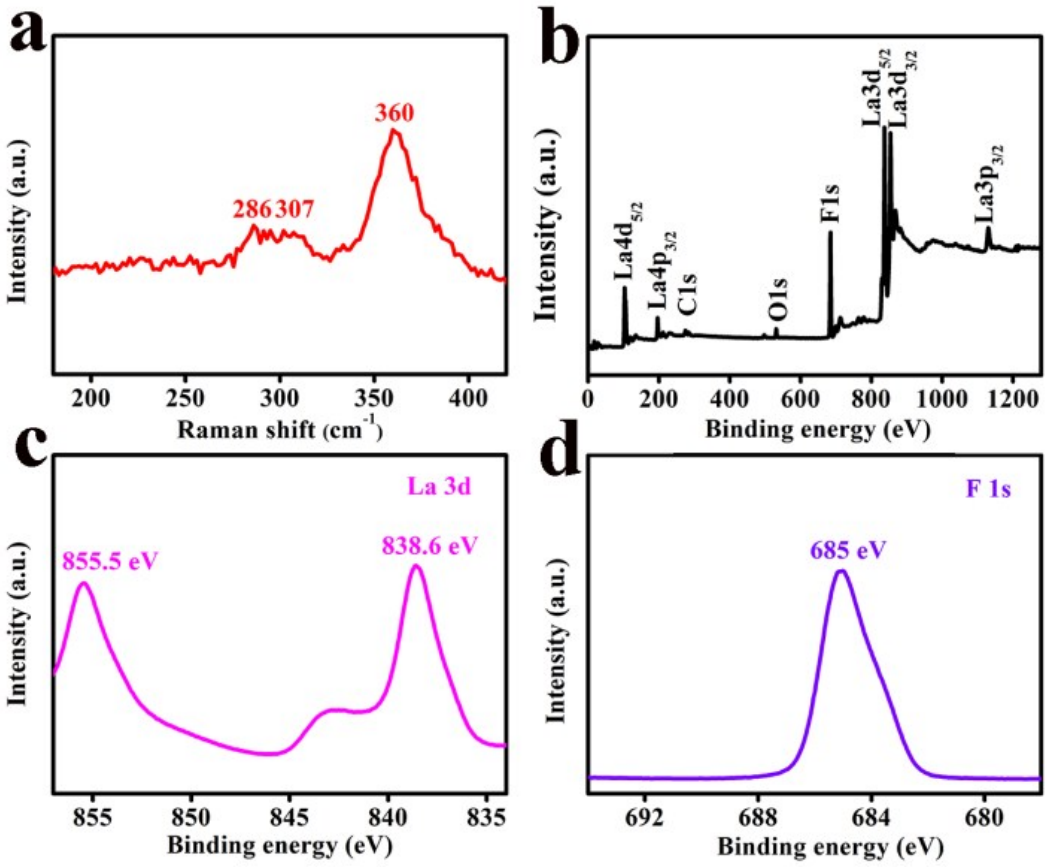

Fig. S3. (a) Raman spectrum for LaF_3. (b) XPS survey spectrum for LaF_3. XPS spectra in the (c) La 3d and (d) F 1s regions for LaF_3.

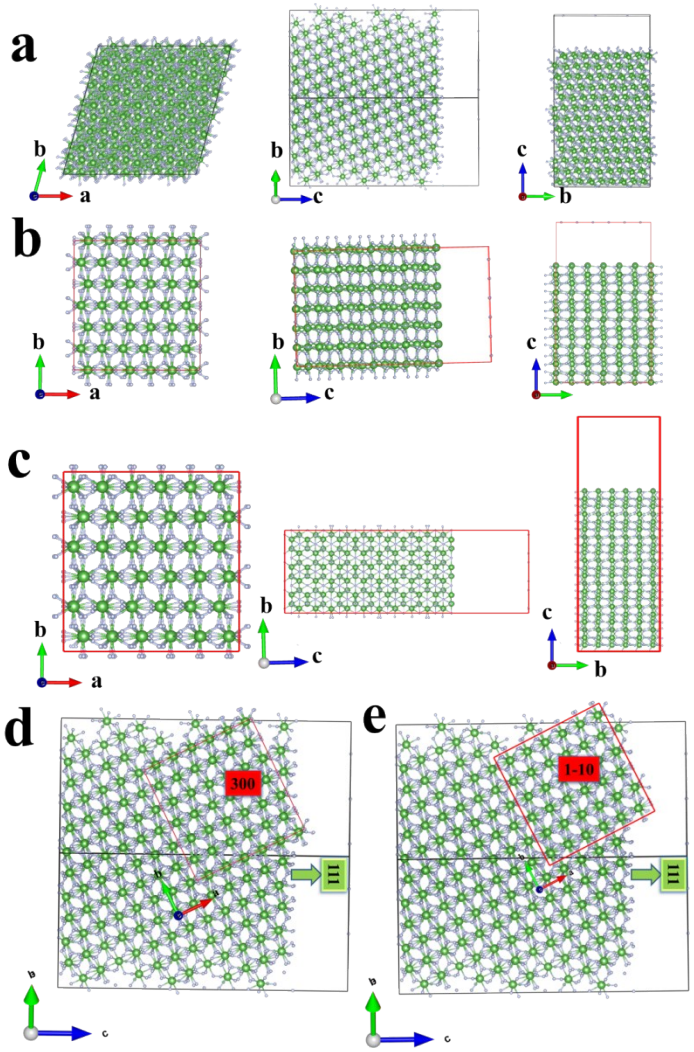

Fig. S4. Atomic three-view of (a) (111), (b) (300), and (c) (1-10) surfaces of LaF_3. Atomic configuration diagram of perfect march of perpendicular between (c) (300) and (111) surface, (d) (1-10), and (111) surface of LaF_3. Based on the HRTEM, SAED and the atom model, the LaF_3 nanoplate preferably grow along the ⟨111⟩ direction. The (111), (300), and (1-10) surfaces are identified as another highly exposed surfaces for the LaF_3 nanoplate according to the angle formula of hexagonal crystal surface and the atomic model, which are perpendicular to the (111) surface.

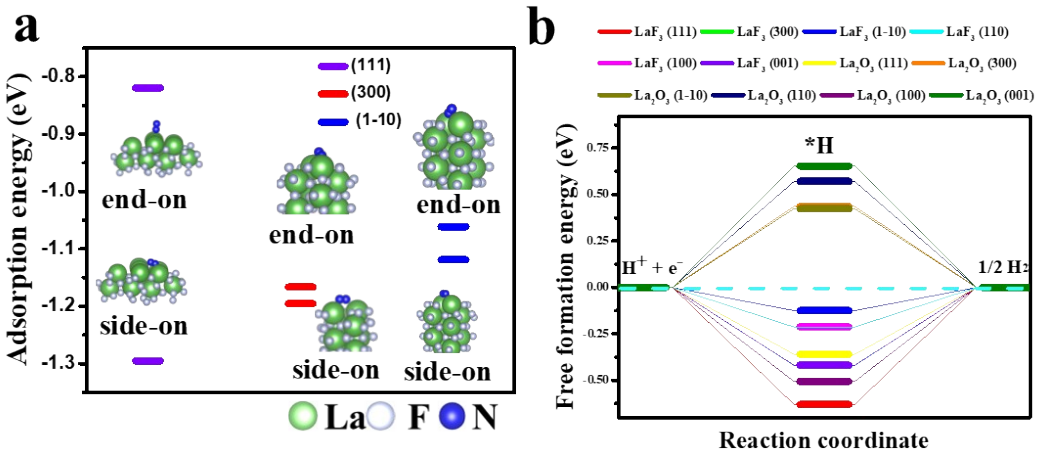

Fig. S5. (a) Calculated N_2 adsorption energy for end-on and side-on configurations on LaF_3 (111), (300), and (1-10) surfaces at 298.15 K. (b) DFT-calculated free energy pathways of HER on the (111), (300), (1-10), (100), (110), and (001) surfaces of LaF_3 and La_2O_3 at surface potential of 0 V under 298.15 K. Insets are the corresponding optimized atomic structures.

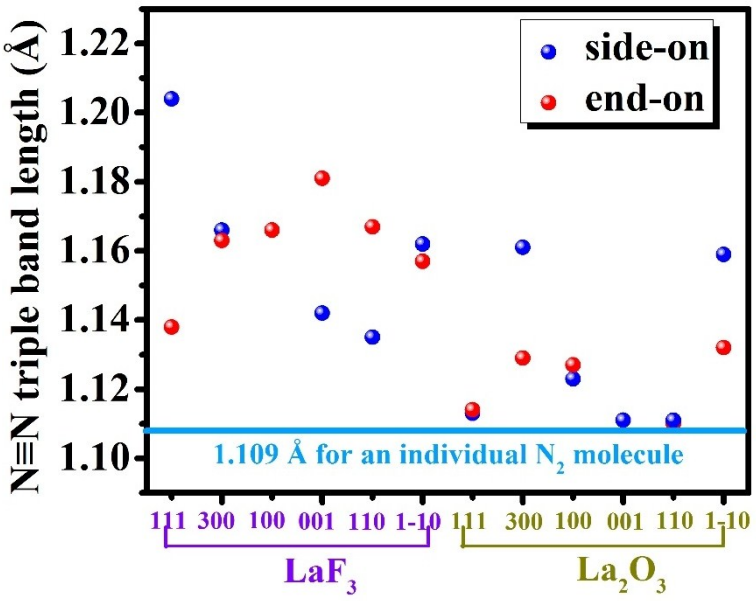

Fig. S6. N≡N triple bond lengths after adsorbed in (111), (300), (1-10), (100), (110), and (001) surfaces of LaF_3 and La_2O_3. The results indicate that LaF_3 exhibits higher N≡N triple bond activation performance than La_2O_3.

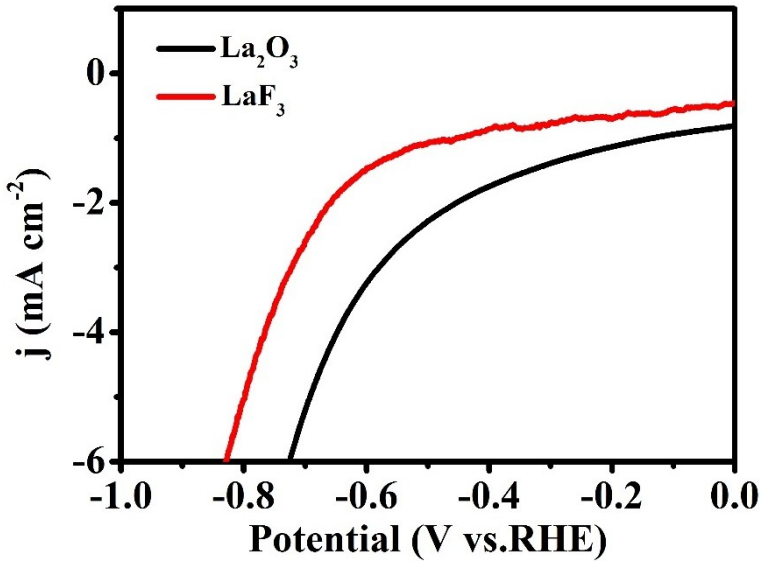

Fig. S7. LSV curves of LaF_3/CP and La_2O_3/CP in Ar-saturated 0.5 M $LiClO_4$ with a scan rate of 2 mV s^{-1}.

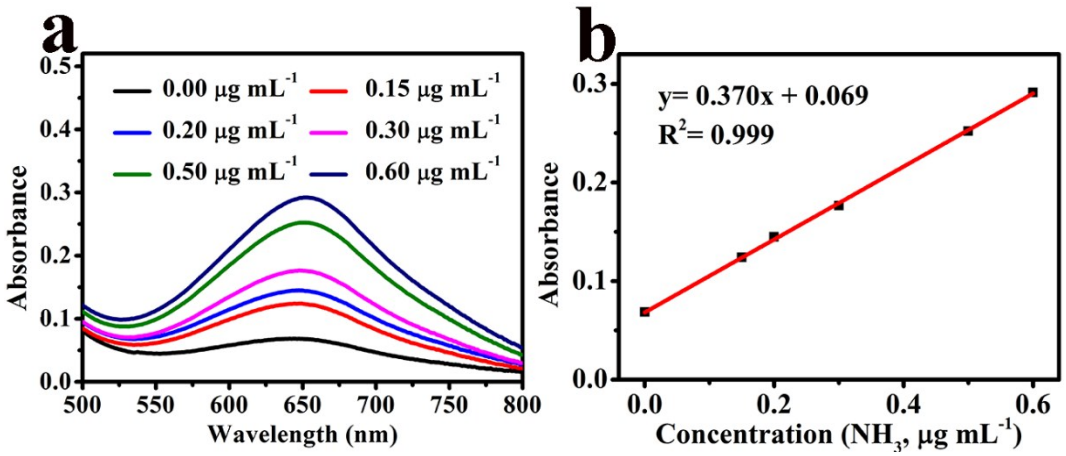

Fig. S8. (a) UV-Vis spectra of various NH_3 concentrations (mother solution: 0.5 M $LiClO_4$) after incubated for 1 h at room temperature. (b) Calibration curve used for calculation of NH_3 concentrations.

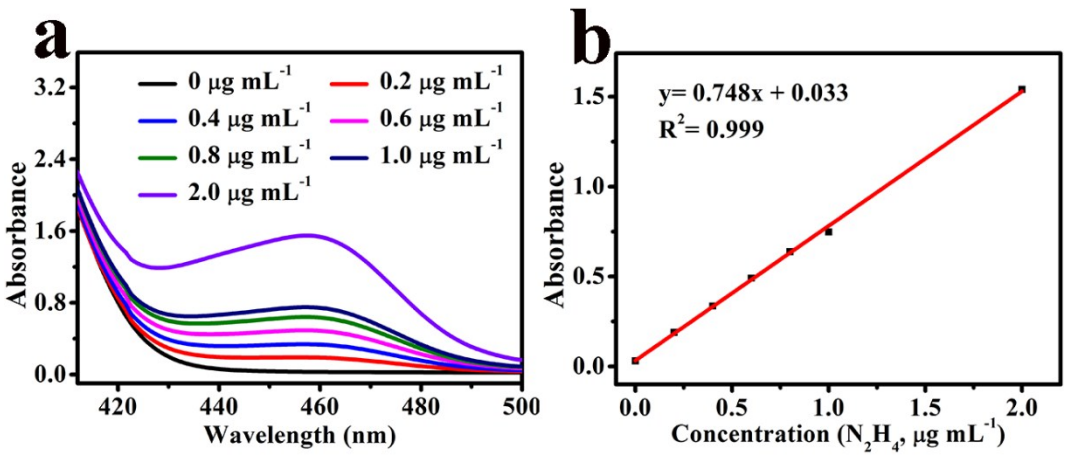

Fig. S9. (a) UV-Vis absorption spectra of various N_2H_4 concentrations after incubated for 20 min at room temperature. (b) Calibration curve used for estimation of N_2H_4 concentration.

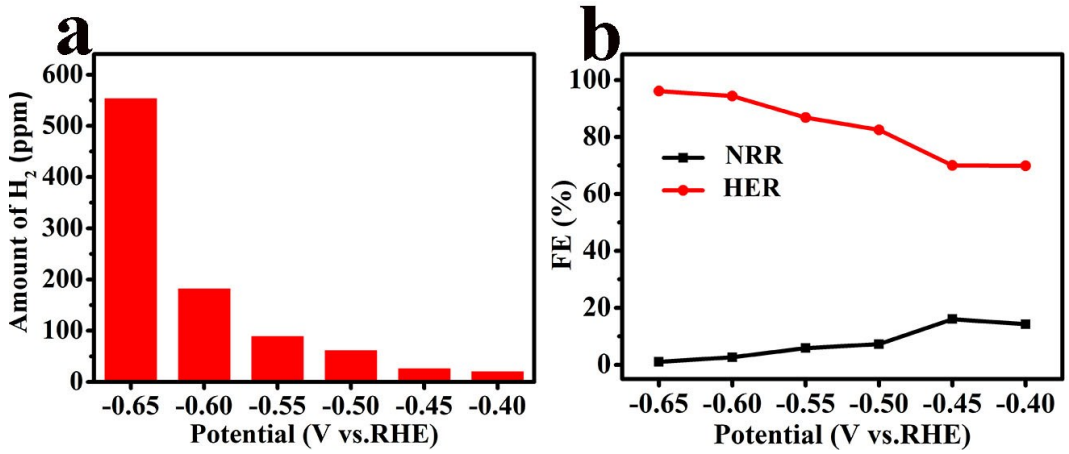

Fig. S10. (a) Amount of evolved H_2 on LaF_3/CP determined by gas chromatography from the headspace of the cell in N_2-saturated 0.5 M $LiClO_4$ at various potentials. (b) The calculated FEs of HER and NRR.

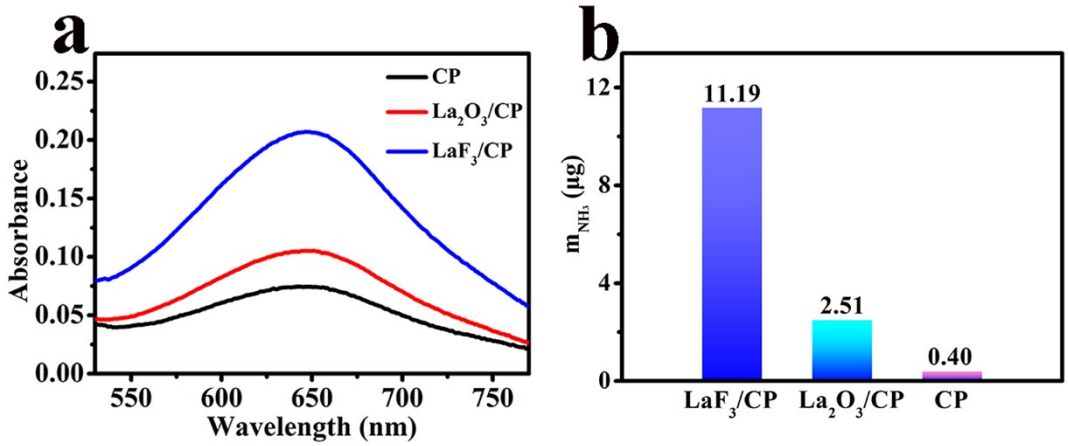

Fig. S11. (a) UV-Vis absorption spectra of the electrolytes coloured with indophenol indicator after electrolysis using different electrodes. (b) Amount of NH_3 generated with bare CP, La_2O_3/CP, and LaF_3/CP at –0.45 V for 2 h.

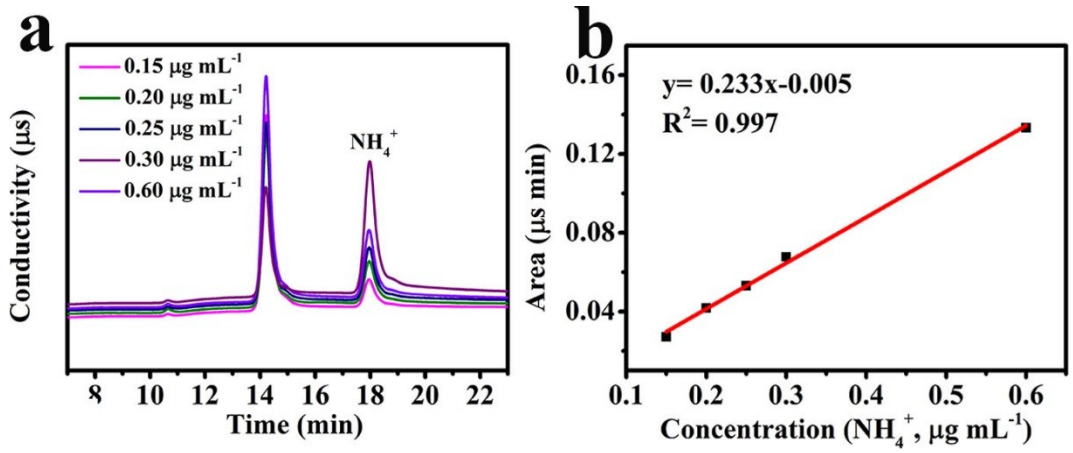

Fig. S12. (a) Ion chromatography data of NH_4^+ with different normal concentrations. (b) The standard curve for the NH_4^+ solution with different content detected by the ion chromatography.

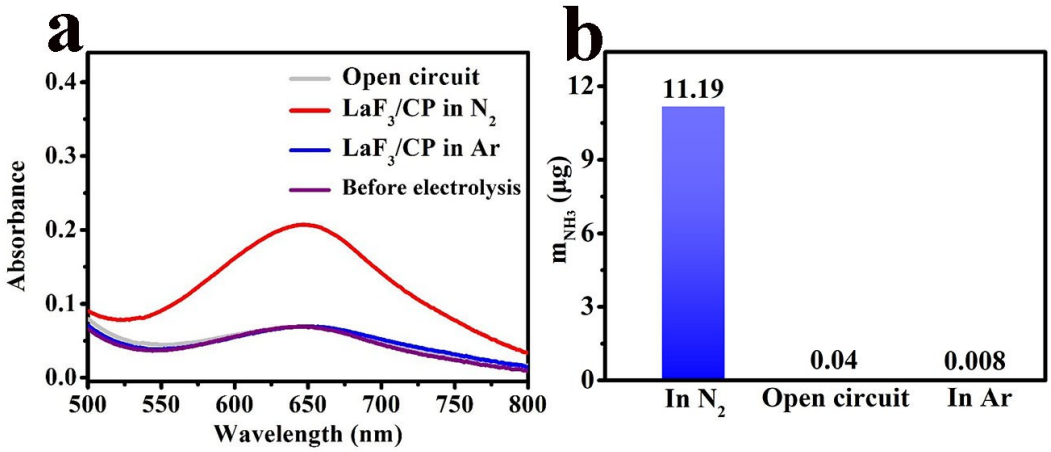

Fig. S13. (a) UV-Vis absorption spectra of the electrolytes stained with indophenol indicator after 2 h electrolysis under different conditions: open circuit in N_2, –0.45 V in N_2, –0.45 V in Ar, and before electrolysis. (b) Amount of NH_3 generated with LaF_3/CP under different conditions.

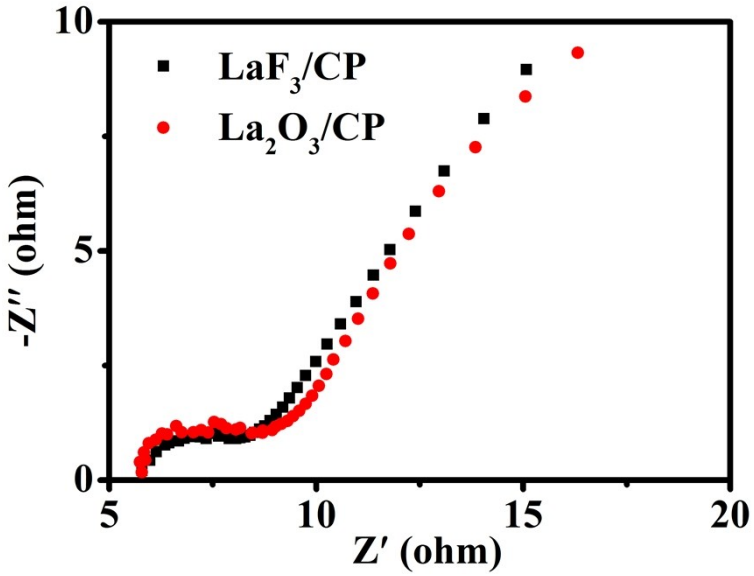

Fig. S14. Nyquist plots of LaF_3/CP and La_2O_3/CP.

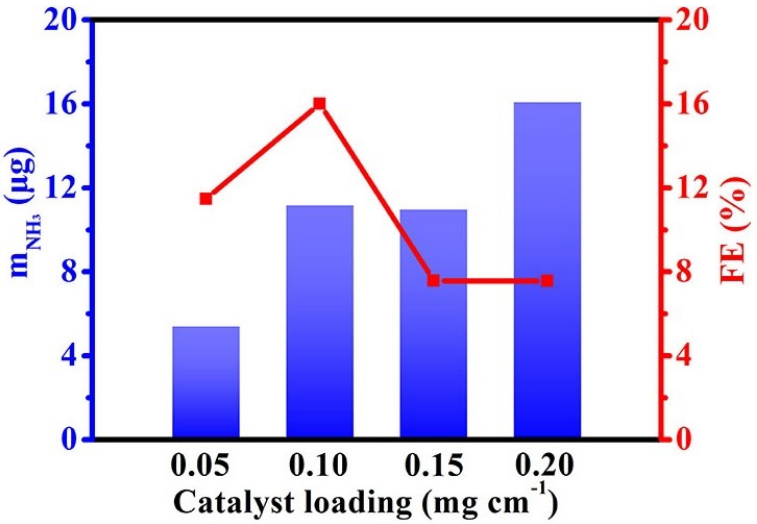

Fig. S15. The amount of NH_3 and FEs for LaF_3/CP with different catalyst loadings.

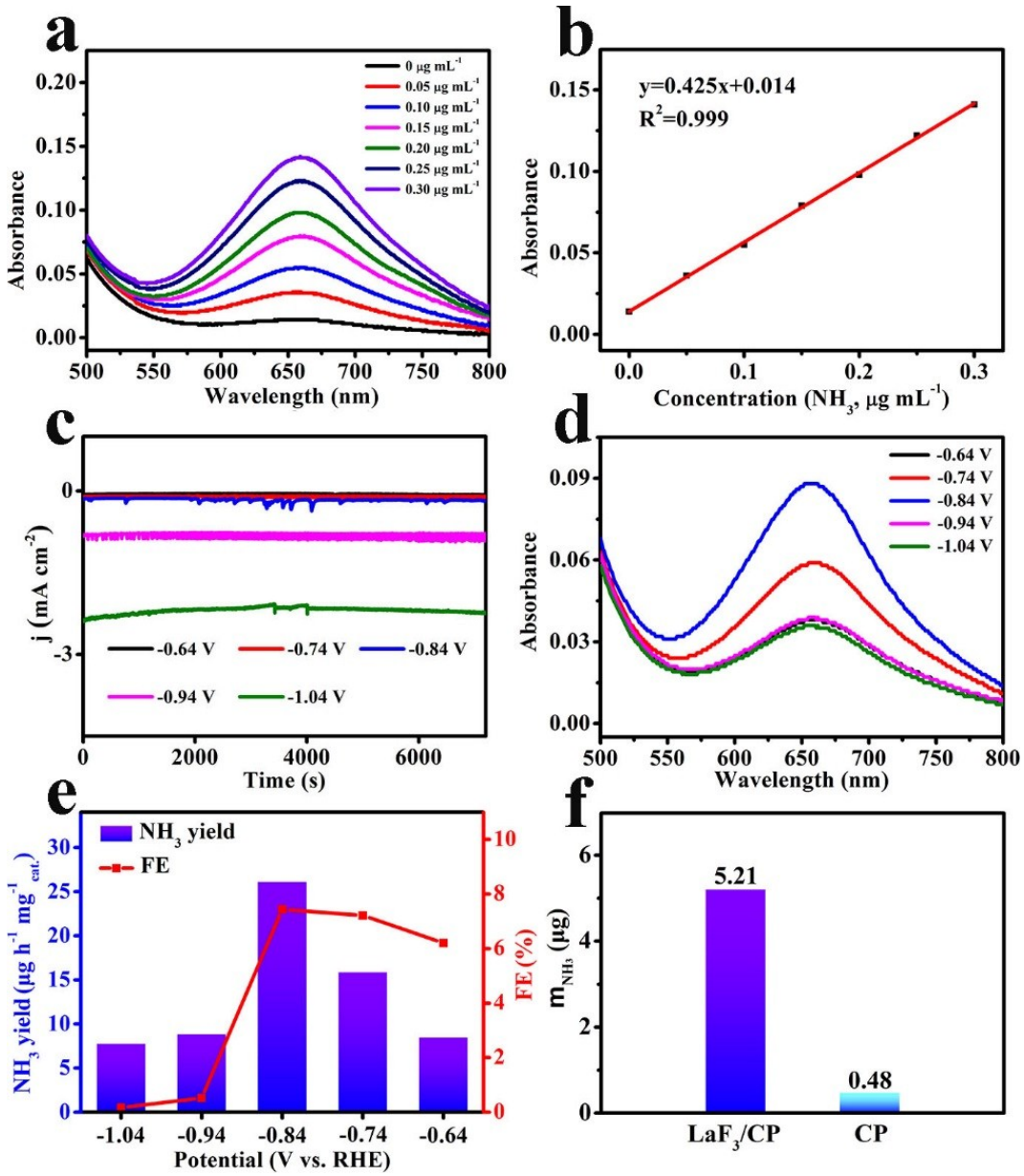

Fig. S16. (a) UV-Vis spectra of indophenol assays with NH_3 concentrations (mother solution: 0.1 M Na_2SO_4) after incubated for 1 h at room temperature. (b) Calibration curve used for calculation of NH_3 concentrations. (c) Time-dependent current density curves of LaF_3/CP at various potentials for 2 h in N_2-saturated 0.1 M Na_2SO_4. (d) UV-Vis absorption spectra of the electrolytes stained with indophenol indicator after NRR electrolysis at a series of potentials for 2 h. (e) NH_3 yield rates and FEs of LaF_3/CP for NRR at different potentials. (f) Amount of NH_3 generated with LaF_3/CP and CP at –0.84 V.

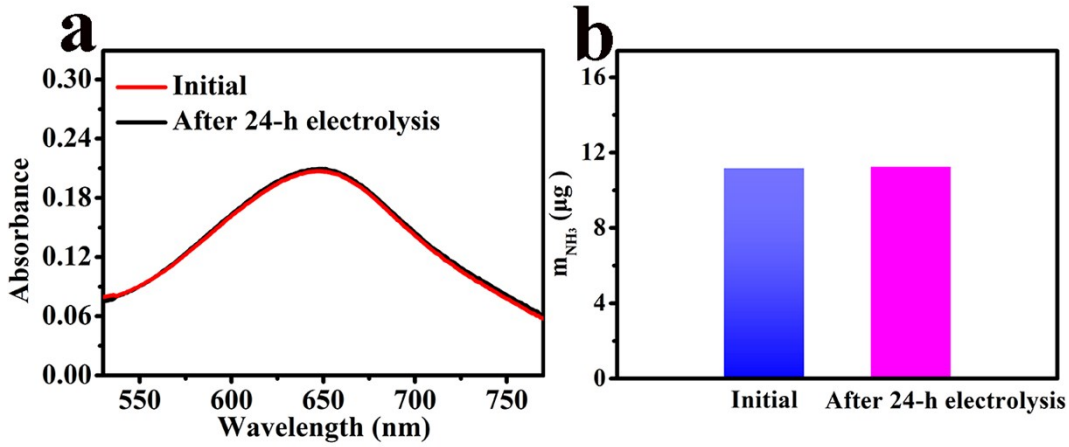

Fig. S17. (a) UV-Vis absorption spectra of the electrolyte stained with indophenol indicator after electrolysis at –0.45 V for 2 h over initial LaF_3/CP and LaF_3/CP subjected to 24 h. (b) Amount of NH_3 generated after 2 h electrolysis over initial LaF_3/CP and LaF_3/CP subjected to 24 h.

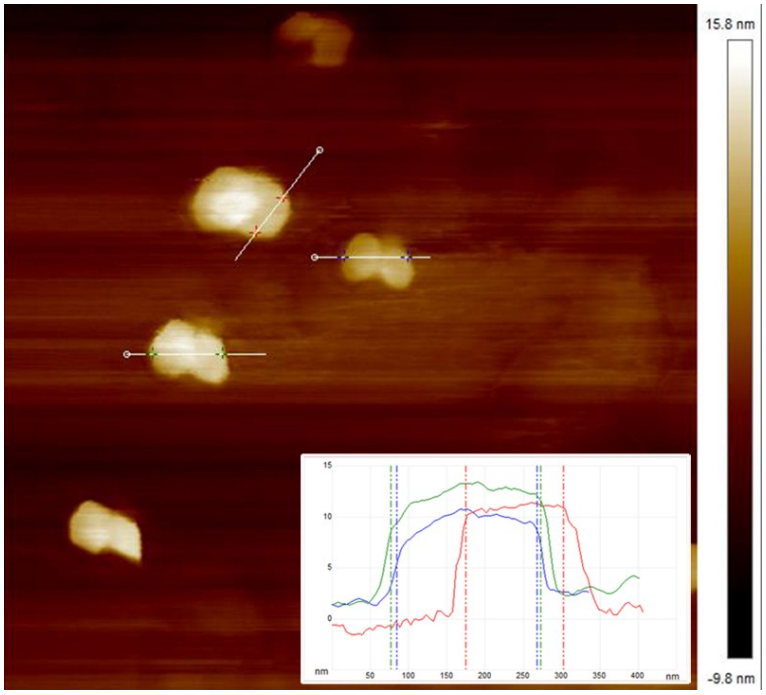

Fig. S18. AFM image and cross-section analysis of LaF_3 nanoplate after stability test.

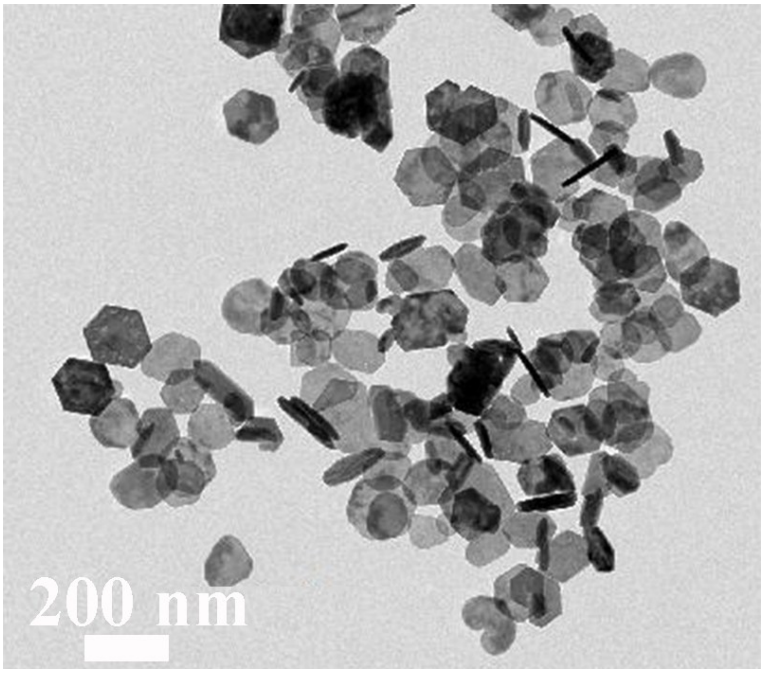

Fig. S19. TEM image of LaF_3 nanoplate after stability test.

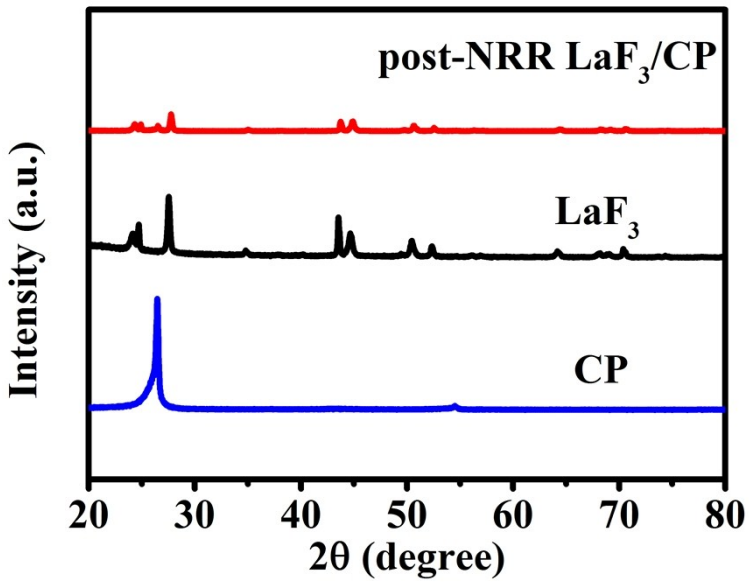

Fig. S20. XRD patterns of LaF_3/CP after stability test.

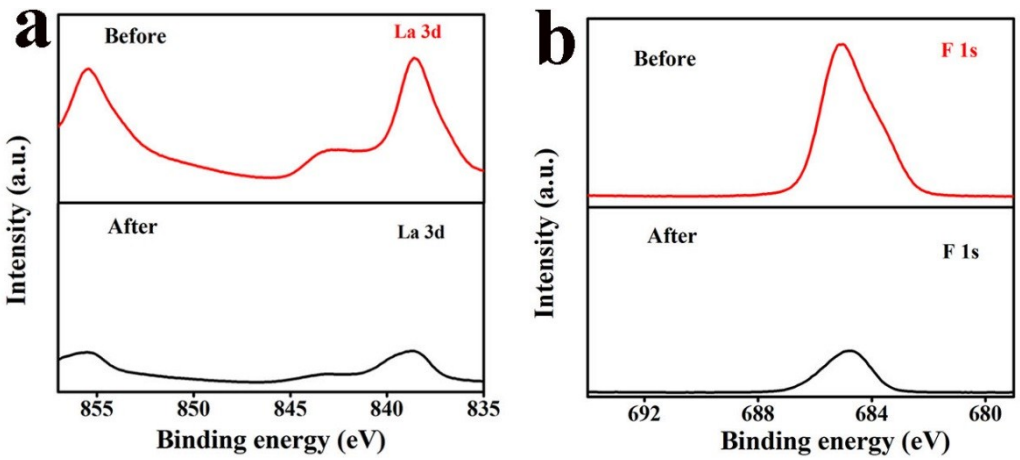

Fig. S21. XPS spectra of LaF_3 in the (a) La 3d and (d) F 1s regions before and after stability test.

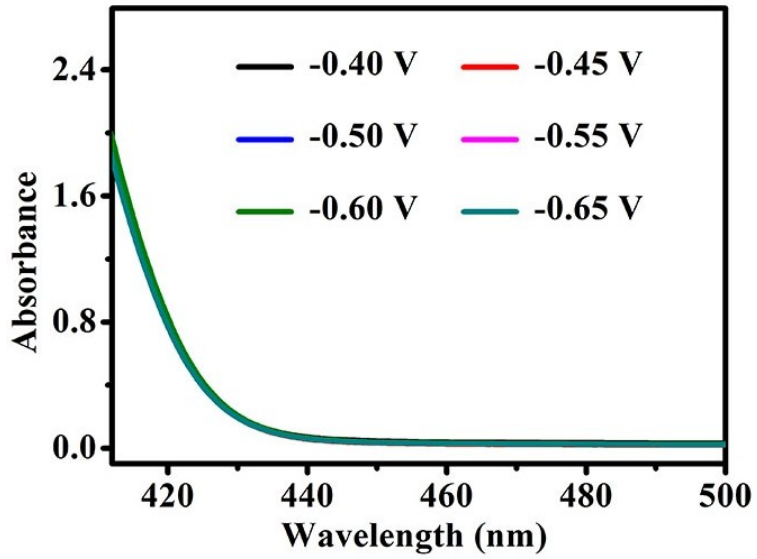

Fig. S22. UV–Vis spectra of the electrolyte estimated by the method of Watt and Chrisp (incubated for 20 min) after 2 h electrolysis at a series of potentials under ambient conditions.

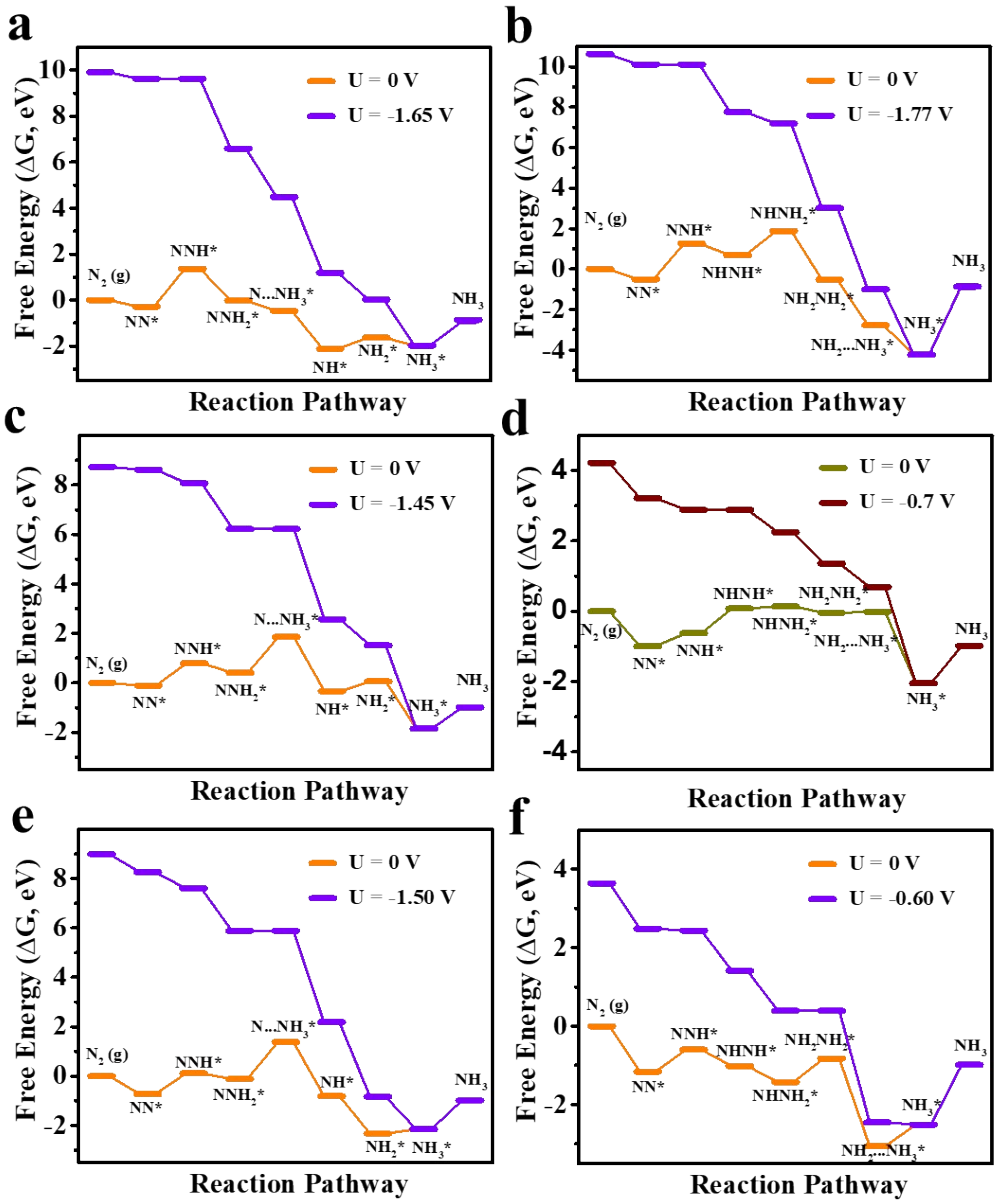

Fig. S23. Free energy diagram for the NRR at zero and applied potential (limiting potential) on La_2O_3 (111) surface through (a) distal and (b) enzymatic mechanisms, on La_2O_3 (300) surface through (c) distal and (d) enzymatic mechanisms and on La_2O_3 (1-10) surface through (e) distal and (f) enzymatic mechanisms.

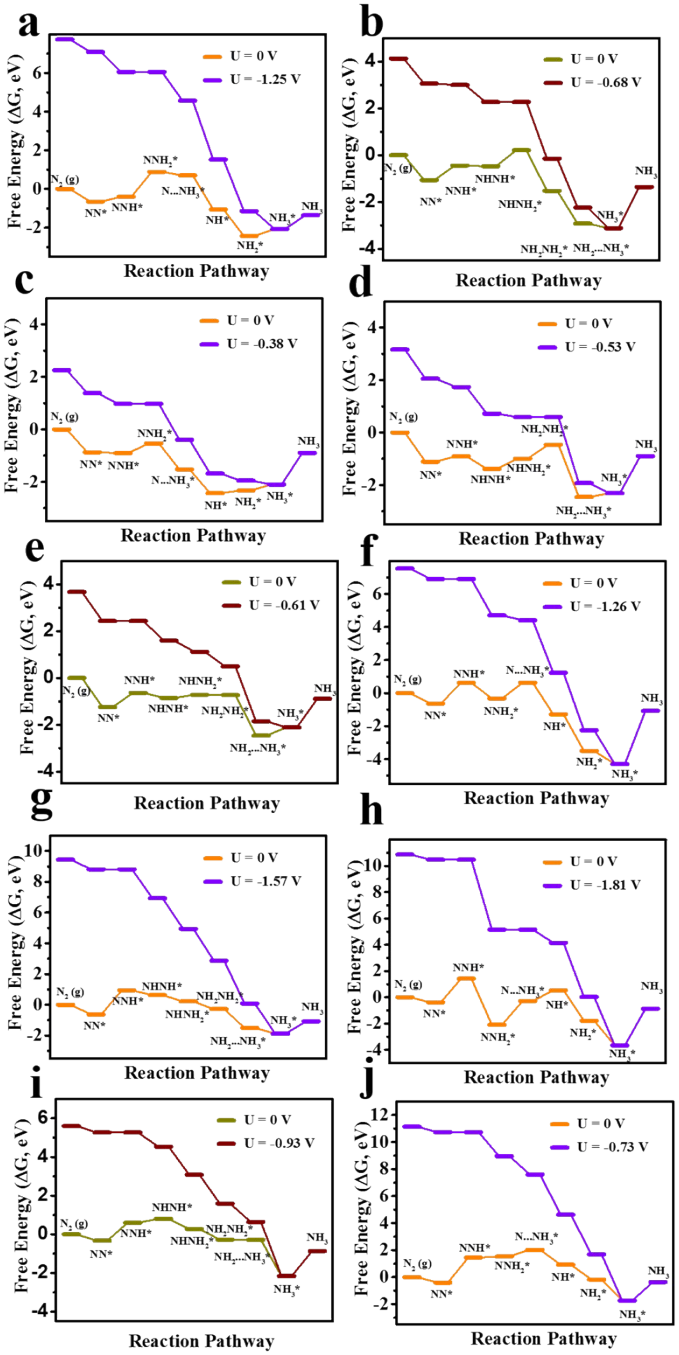

Fig. S24. Free energy diagram for the NRR at zero and applied potential (limiting potential) on LaF_3 (110) surface through (a) distal and (b) enzymatic mechanisms, LaF_3 (001) surface through (c) distal and (d) enzymatic mechanisms, LaF_3 (100) surface through (e) enzymatic mechanisms, La_2O_3 (110) surface through (f) distal and (g) enzymatic mechanisms, La_2O_3 (100) surface through (h) distal and (i) enzymatic mechanisms, and on La_2O_3 (001) surface through (j) distal mechanisms.

Table S1. Comparison of the catalytic performances of LaF_3/CP with other non-noble-metal NRR catalysts at ambient conditions.

Catalyst	Electrolyte	NH_3 yield	FE (%)	Ref.
LaF_3/CP	0.5 M $LiClO_4$	55.9 μg h^{-1} $mg^{-1}_{cat.}$	16.0	This work
		9.1×10^{-11} mol $s^{-1}cm^{-2}$		
		5.59 μg h^{-1} cm^{-2}		
β-FeOOH	0.5 M $LiClO_4$	23.32 μg h^{-1} $mg^{-1}_{cat.}$	6.7	7
MXene/SSM	0.5 M Li_2SO_4	4.72 μg h^{-1} cm^{-2}	4.62	8
PEBCD/C	0.5 M Li_2SO_4	1.58 μg h^{-1} cm^{-2}	2.85	9
Mn_3O_4	0.1 M Na_2SO_4	11.6 μg h^{-1} $mg^{-1}_{cat.}$	3.0	10
VO_2 hollow microsphere	0.1 M Na_2SO_4	14.85 μg h^{-1} $mg^{-1}_{cat.}$	3.97	11
TiO_2	0.1 M Na_2SO_4	9.16×10^{-11} mol $s^{-1}\cdot cm^{-2}$	2.5	12
SnO_2	0.1 M Na_2SO_4	1.47×10^{-10} mol s^{-1} cm^{-2}	2.17	13
Fe_3O_4/Ti	0.1 M Na_2SO_4	5.6×10^{-11} mol s^{-1} cm^{-2}	2.6	14
hollow Cr_2O_3	0.1 M Na_2SO_4	25.3 μg h^{-1} $mg^{-1}_{cat.}$	6.78	15
MoS_2/CC	0.1 M Na_2SO_4	8.08×10^{-11} mol s^{-1} cm^{-2}	1.17	16
S-doped carbon nanosphere	0.1 M Na_2SO_4	19.07 μg h^{-1} $mg^{-1}_{cat.}$	7.47	17
defect-rich fluorographene	0.1 M Na_2SO_4	9.3 μg h^{-1} $mg^{-1}_{cat.}$	4.2	18
CoO quantum dots	0.1 M Na_2SO_4	21.5 μg h^{-1} $mg^{-1}_{cat.}$	8.3	19
Fe_2O_3-CNT	$KHCO_3$	3.58×10^{-12} mol s^{-1} cm^{-2}	0.15	20
N-doped porous carbon	0.05 M H_2SO_4	23.8 μg h^{-1} $mg^{-1}_{cat.}$	1.42	21
(110)-oriented Mo nanofilm	0.01 M H_2SO_4	3.09×10^{-11} mol s^{-1} cm^{-2}	0.72	22
$Bi_4V_2O_{11}$/CeO_2	0.1 M HCl	23.21 μg h^{-1} $mg^{-1}_{cat.}$	10.16	23
Nb_2O_5 nanofiber	0.1 M HCl	43.6 μg h^{-1} $mg^{-1}_{cat.}$	9.26	24
B_4C	0.1 M HCl	26.57 μg h^{-1} $mg^{-1}_{cat.}$	15.95	25

Fe_3S_4	0.1 M HCl	75.4 μg h^{-1} $mg^{-1}_{cat.}$	6.45	26
C_3N_4	0.1 M HCl	8.09 μg h^{-1} $mg^{-1}_{cat.}$	11.59	27
Mo_2C nanorod	0.1 M HCl	95.1 μg h^{-1} $mg^{-1}_{cat.}$	8.13	28
N-doped porous carbon	0.1 M HCl	15.7 μg h^{-1} $mg_{cat.}^{-1}$	1.45	29
sulfur-doped graphene	0.1 M HCl	27.3 μg h^{-1} cm^{-2}	11.5	30
NP-C-MOF-5	0.1 M HCl	1.08 μg h^{-1} $mg^{-1}_{cat.}$	-	31
γ-Fe_2O_3	0.1 M KOH	0.212 μg h^{-1} $mg^{-1}_{cat.}$	1.9	32
CoP hollow nanocage	1.0 M KOH	10.78 μg h^{-1} $mg^{-1}_{cat.}$	7.36	33
Fe/Fe_3O_4	0.1 M PBS	3.10×10^{-12} mol s^{-1} cm^{-2}	8.29	34

References

1 D. Zhu, L. Zhang, R. E. Ruther and R. J. Hamers, *Nat. Mater.*, 2013, **12**, 836–841.

2 G. W. Watt and J. D. Chrisp, *Anal. Chem.*, 1952, **24**, 2006–2008.

3 B. J. Delley, *J. Chem. Phys.*, 1990, **92**, 508–517.

4 J. P. Perdew, K. Burke and M. Ernzerhof, *Phys. Rev. Lett.*, 1996, **77**, 3865–3868.

5 B. Delley, *J. Chem. Phys.*, 2000, **113**, 7756–7764.

6 N. Govind, M. Petersen, G. Fitzgerald, D. King-Smith and J. Andzelm, *Comput. Mater. Sci.*, 2003, **28**, 250–258.

7 X. Zhu, Z. Liu, Q. Liu, Y. Luo, X. Shi, A. M. Asiri, Y. Wu and X. Sun, *Chem. Commun.*, 2018, **54**, 11332–11335.

8 Y. Luo, G. Chen, L. Ding, X. Chen, L. Ding and H. Wang, *Joule*, 2019, **3**, 1–11.

9 G.-F. Chen, X. Cao, S. Wu, X. Zeng, L. Ding, M. Zhu and H. Wang, *J. Am. Chem. Soc.*, 2017, **139**, 9771–9774.

10 X. Wu, L. Xia, Y. Wang, W. Lu, Q. Liu, X. Shi and X. Sun, *Small*, 2018, **14**, 1803111.

11 R. Zhang, H. Guo, L. Yang, Y. Wang, Z. Niu, H. Huang, H. Chen, L. Xia, T. Li, X. Shi, X. Sun, B. Li and Q. Liu, *ChemElectroChem*, 2019, **6**, 1014–1018.

12 R. Zhang, X. Ren, X. Shi, F. Xie, B. Zheng, X. Guo and X. Sun, *ACS Appl. Mater. Interfaces*, 2018, **10**, 28251–28255.

13 L. Zhang, X. Ren, Y. Luo, X. Shi, A. M. Asiri, T. Li and X. Sun, *Chem. Commun.*, 2018, **54**, 12966–12969.

14 Q. Liu, X. Zhang, B. Zhang, Y. Luo, G. Cui, F. Xie and X. Sun, *Nanoscale*, 2018, **10**, 14386–14389.

15 Y. Zhang, W. Qiu, Y. Ma, Y. Luo, Z. Tian, G. Cui, F. Xie, L. Chen, T. Li and X. Sun, *ACS Catal.*, 2018, **8**, 8540–8544.

16 L. Zhang, X. Ji, X. Ren, Y. Ma, X. Shi, Z. Tian, A. M. Asiri, L. Chen, B. Tang and X. Sun, *Adv. Mater.*, 2018, **30**, 1800191.

17 L. Xia, X. Wu, Y. Wang, Z. Niu, Q. Liu, T. Li, X. Shi, A. M. Asiri and X. Sun, *Small Methods*, 2018, **14**, 1800251.

18 J. Zhao, J. Yang, L. Ji, H. Wang, H. Chen, Z. Niu, Q. Liu, T. Li, G. Cui and X. Sun, *Chem. Commun.*, 2019, **55**, 4266–4269.

19 K. Chu, Y. Liu, Y. Li, H. Zhang and Y. Tian, *J. Mater. Chem. A*, 2019, **7**, 4389–4394.

20 S. Chen, S. Perathoner, C. Ampelli, C. Mebrahtu, D. Su and G. Centi, *Angew. Chem., Int. Ed.*, 2017, **56**, 2699–2703.

21 Y. Liu, Y. Su, X. Quan, X. Fan, S. Chen, H. Yu, H. Zhao, Y. Zhang and J. Zhao, *ACS*

Catal., 2018, **8**, 1186−1191.

22 D. Yang, T. Chen and Z. Wang, *J. Mater. Chem. A*, 2017, **5**, 18967–18971.

23 C. Lv, C. Yan, G. Chen, Y. Ding, J. Sun, Y. Zhou and G. Yu, *Angew. Chem.*, *Int. Ed.*, 2018, **57**, 6073–6076.

24 J. Han, Z. Liu, Y. Ma, G. Cui, F. Xie, F. Wang, Y. Wu, S. Gao, Y. Xu and X. Sun, *Nano Energy*, 2018, **52**, 264–270.

25 W. Qiu, X. Xie, J. Qiu, W. Fang, R. Liang, X. Ren, X. Ji, G. Cui, A. M. Asiri, G. Cui, B. Tang and X. Sun, *Nat. Commun.*, 2018, **9**, 3485.

26 X. Zhao, X. Lan, D. Yu, H. Fu, Z. Liu and T. Mu, *Chem. Commun.*, 2018, **54**, 13010–13013.

27 C. Lv, Y. Qian, C. Yan, Y. Ding, Y. Liu, G. Chen and G. Yu, *Angew. Chem.*, *Int. Ed.*, 2018, **57**, 10246–10250.

28 X. Ren, J. Zhao, Q. Wei, Y. Ma, H. Guo, Q. Liu, Y. Wang, G. Cui, A. M. Asiri, B. Li, B. Tang and X. Sun, *ACS Central Sci.*, 2019, **5**, 116–121.

29 X. Yang, K. Li, D. Cheng, W. Pang, J. Lv, X. Chen, H. Zang, X. Wu, H. Tan, Y. Wang and Y. Li, *J. Mater. Chem. A*, 2018, **6**, 7762–7769.

30 L. Xia, J. Yang, H. Wang, R. Zhao, H. Chen, W. Fang, A. M. Asiri, F. Xie, G. Cui and X. Sun, *Chem. Commun.*, 2019, **55**, 3371–3374.

31 P. Song, L. Kang, H. Wang, R. Guo and R. M. Wang, *ACS Appl. Mater. Interfaces*, 2019, **11**, 12408−12414.

32 J. Kong, A. Lim, C. Yoon, J. H. Jang, H. C. Ham, J. Han, S. Nam, D. Kim, Y.-E. Sung, J. Choi and H. S. Park, *ACS Sustainable Chem. Eng.*, 2017, **5**, 10986–10995.

33 W. Guo, Z. Liang, J. Zhao, B. Zhu, K. Cai, R. Zou and Q. Xu, *Small Methods*, 2018, **2**, 1800204.

34 L. Hu, A. Khaniya, J. Wang, G. Chen, W. E. Kaden and X. Feng, *ACS Catal.*, 2018, **8**, 9312–9319.